ITU Journal
Future and evolving technologies

ITU Journal on Future and Evolving Technologies, Volume 6, Issue 2, June 2025

Article

Phase-continuous multi-BS signal aggregation for range estimation in ISAC systems

Yi Geng [1]

[1] *CICT Mobile, China*

Corresponding author: Yi Geng, gengyi@cictmobile.com

Achieving high-precision ranging in Integrated Sensing and Communications (ISAC) systems operating in low-frequency bands is challenging due to fragmented frequency resources and clock synchronization errors across multiple operators. Cross-operator Carrier Aggregation (CA) offers a potential solution by combining fragmented frequency resources, but clock synchronization errors between Base Stations (BSs) cause phase discontinuities that severely degrade ranging performance. This paper proposes a novel method for cross-operator CA scenarios that leverages successive echo signals to mitigate these phase discontinuities without requiring perfect clock synchronization between BSs. A comprehensive mathematical analysis of phase discontinuities in multi-BS systems is provided and their impact on range profiles is quantified, revealing a characteristic "fishbone effect" that substantially reduces ranging accuracy. Our proposed method effectively eliminates this effect by progressively matching phase transitions between signals from different BSs. Through extensive simulations in both single-target and multi-target scenarios, the proposed method achieves similar range accuracy comparable to systems under perfect synchronization conditions, offering a viable solution for applications requiring accurate positioning in resource-constrained environments.

Keywords: Carrier aggregation, clock synchronization error, high-precision ranging, IFFT algorithm, ISAC, OFDM, phase synchronization

1. INTRODUCTION

With the advent of 6G, Integrated Sensing and Communications (ISAC) has become a cornerstone for enabling advanced applications such as autonomous driving, industrial automation, and augmented reality [1, 2, 3]. These applications rely on extremely accurate range measurements, which require continuous and wide frequency bandwidths [4]. However, achieving such bandwidths in lower frequency bands is challenging due to limited spectrum availability and fragmented allocations among multiple operators. For instance, as shown in Fig. 1, the NR bands n77 and n78 (3.6-4.1 GHz) allocated for 5G in Japan are divided among several operators, with each operator receiving only a small portion. This fragmented allocation leaves no single operator with sufficient continuous bandwidth to support high-precision ranging. Although higher frequency bands offer larger bandwidths, they suffer from severe path loss, significantly limiting the effective range of ISAC systems [5, 6].

Carrier Aggregation (CA) is an intuitive solution to address the fragmented frequency resource problem, it is a widely-used technique to combine bandwidths from different frequency bands, enabling the creation of wideband resources [7, 8]. CA includes three types: intra-band contiguous CA, intra-band non-contiguous CA, and inter-band non-contiguous CA [9], as illustrated in Fig. 2. These three types of CA can be implemented using different hardware architectures. Fig. 3 illustrates three hardware architectures according to where Component Carriers (CC) are combined. Fig. 3a depicts architecture 1: a Single Baseband with a Single RF Chain (SBSC); Fig. 3b shows architecture 2: Multiple Basebands with a Single RF Chain (MBSC); Fig. 3c illustrates architecture 3: Multiple Basebands with Multiple RF Chains (MBMC) [9].

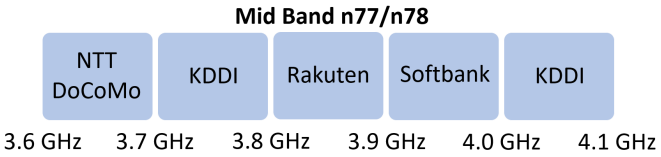

Figure 1 – Mid-band spectrum allocation (3.6-4.1 GHz) among operators in Japan for 5G networks.

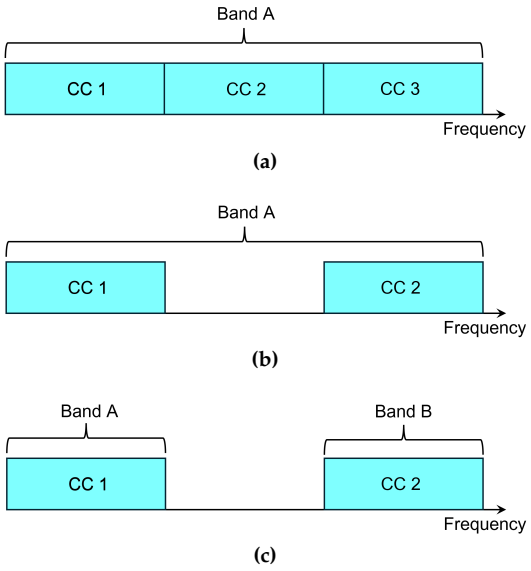

Figure 2 – The types of CA. (a) Intra-band contiguous CA. (b) Intra-band non-contiguous CA. (c) Inter-band non-contiguous CA.

For SBSC architecture, since the clocks for different CCs come from the same baseband and the same RF chain, the CCs can be considered perfectly synchronized. For MBSC and MBMC architectures, since the clocks for different CCs come from different basebands and different RF chains, clock errors exist between CCs, typically at the nanosecond level. Intra-band contiguous CA can utilize any of these architectures, intra-band non-contiguous CA can utilize MBSC and MBMC architectures, while inter-band non-contiguous CA can only utilize the MBMC architecture.

For CA with communication purposes, all three hardware architectures are suitable, as nanosecond-level clock errors between CCs do not affect symbol synchronization. For CA with sensing purposes, when concatenating echo signals from different CCs, phase continuity must be maintained at the junction points, meaning phase jumps cannot occur, as they would severely impact sensing performance [10]. Since cellular network signals have extremely short periods (for example, a 3.7 GHz signal has a period of only 270 ps), clock errors between CCs must be controlled to the picosecond level to ensure signal phase continuity. Currently, there is limited research on phase jumps between echo signals after CA [11]. In [7], Wei et al. suggest that for intra-band contiguous CA with SBSC architecture, since CCs can be considered perfectly synchronized, echo signals from different CCs can be directly concatenated without considering phase jumps.

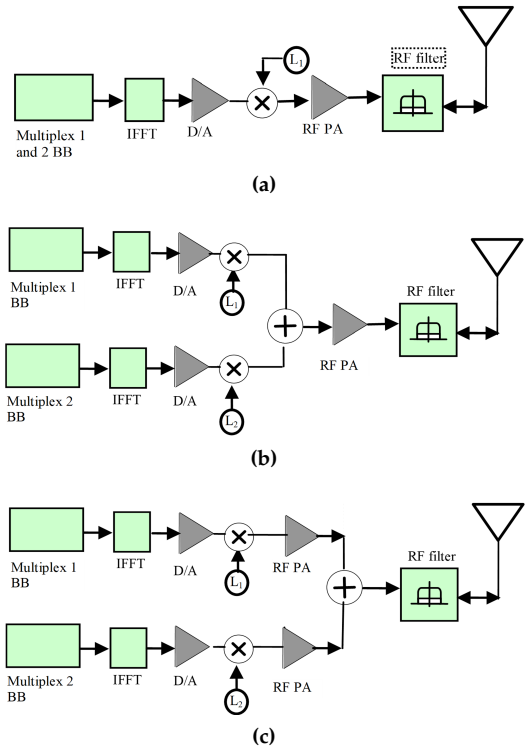

Figure 3 – Hardware architectures for CA. (a) SBSC. (b) MBSC. (c) MBMC.

The stepped-carrier OFDM radar scheme proposed by Schweizer et al. [12] only addresses the phase jump issues caused by target motion during the time intervals between transmitted CCs, without addressing the phase discontinuities resulting from clock errors between different CCs. Their approach assumes all CCs share the same clock source, corresponding to the SBSC architecture, but does not consider how clock errors between different baseband and RF chains in MBSC and MBMC architectures affect CA sensing performance. In the context of CA-enabled ISAC systems, Wei et al. [7] proposed a staggered pilot structure that aggregates high and low-frequency bands to improve sensing performance. While their approach demonstrates enhanced range and velocity estimation accuracy through simulation, it fails to address the phase discontinuities between CCs resulting from clock errors between separate basebands and RF chains. Their signal processing algorithm focuses on combining channel information matrices with different subcarrier spacings but overlooks the phase jumps that would occur at carrier junctions in practical hardware deployments. This limitation significantly restricts the applicability of their method in real-world ISAC systems.

To address these challenges in CA for sensing, a thorough analysis of the effects of clock errors on phase jumps between CCs is essential, yet absent in existing literature. Current approaches neither analyse the impact of these phase discontinuities on sensing performance nor provide practical solutions to mitigate them. This issue becomes particularly critical in inter-operator CA scenarios,

where CCs not only come from different RF chains and basebands but also from entirely separate operator networks with independent timing references. The resulting phase jumps can severely degrade range accuracy, effectively nullifying the potential benefits of bandwidth aggregation for sensing applications. Innovative solutions are urgently needed to achieve high-precision ranging in low-frequency bands, despite fragmented bandwidth allocations. This paper addresses this critical gap by proposing a novel method to aggregate non-contiguous frequency resources across multiple operators, effectively forming a wideband spectrum in the low frequency spectrum while compensating for the phase discontinuities introduced by independent clock sources.

The organization of this paper is as follows: Section 2 compares data-level fusion and signal-level fusion approaches in cooperative sensing, highlighting the challenges of achieving signal-level fusion in multi-BS systems. Section 3 presents a comprehensive mathematical analysis of CA with both perfect and imperfect clock synchronization, identifying the "fishbone effect" that emerges from phase discontinuities. Section 4 introduces our proposed method for mitigating phase discontinuities using subsequent echo signals, including a detailed analysis of the phase matching process and associated delay. Section 5 provides extensive simulation results for both single-target and multi-target scenarios, demonstrating the effectiveness of our approach in improving range and location accuracy. Finally, Section 6 concludes the paper and outlines future research directions.

2. SENSING INFORMATION FUSION IN COOPERATIVE SENSING

In Section 1, multiple Base Stations (BSs) using CA for large bandwidth sensing was considered, which essentially constitutes a scenario of cooperative sensing. Cooperative sensing involves multiple ISAC nodes individually measuring a target and fusing their sensing information to enhance sensing performance. There are two levels of sensing information fusion between different ISAC nodes: data-level fusion and signal-level fusion [13, 14].

Data-level fusion involves each ISAC node processing the received echo signals reflected from targets to obtain sensing results, such as range, velocity, and angle. These results are then transmitted to a Sensing Processing Unit (SPU), which combines the sensing results from different ISAC nodes (e.g., using clustering algorithms) to derive the final sensing results. Data-level fusion offers advantages like low complexity and reduced data transmission between ISAC nodes and SPU. However, clock synchronization error between nodes can affect the fusion results. For instance, a clock synchronization error of 1 nanosecond can lead to a range error of 15 centimeters. When multiple BSs employ data-level fusion for sensing, the improvement in sensing performance is limited because each BS uses its individual bandwidth, therefore the range accuracy and resolution cannot be effectively increased.

Signal-level fusion, on the other hand, entails transmitting the raw echo signals received by each ISAC node directly to the SPU. The SPU then fuses and processes these raw echo signals from different nodes to obtain the final sensing results. Because signal-level fusion utilizes the original signals without introducing additional signal processing errors, it theoretically yields the optimal sensing results. However, no practical signal-level fusion solutions exist yet for ISAC systems [15]. The primary challenge lies in the requirement of extremely precise phase synchronization for fusing echo signals from different ISAC nodes. For instance, in the scenario depicted in Fig. 1, where BSs from operators DoCoMo and KDDI engage in cooperative ranging via CA, the band boundary is 3.7 GHz, corresponding to a wave period of 270 picoseconds. If the phase error at the junction needs to be less than 0.01π radians, the clock synchronization error between two BSs must be less than 1.35 picoseconds. Achieving such clock precision is practically impossible in cellular networks.

Signal-level fusion is only achieved in Distributed Aperture Coherence synthetic Radars (DACRs). Coherent accumulation in DACR is a technique that combines echo signals from multiple radars to increase the echo signal-to-noise ratio and enhance target detection [16]. However, in DACR, all radars must transmit signals at the same frequency and bandwidth. Therefore, bandwidth cannot be expanded through CA to improve range resolution and accuracy. As such, coherent accumulation technology in DACR is not applicable to scenarios involving multiple BSs using CA and signal-level fusion for cooperative sensing.

To better understand the differences between data-level fusion and signal-level fusion, their characteristics are compared in Table 1. Based on the analysis above, to significantly enhance range sensing performance through CA, it is essential to use signal-level fusion to integrate echo signals from different BSs. The requirement for picosecond-level clock synchronization between BSs poses the greatest challenge to this approach.

Table 1 – Comparison of data-level fusion and signal-level fusion

Characteristics	Data-level fusion	Signal-level fusion
Sensing information to fuse	sensing results	raw echo signals
Complexity	Low	High
Data transmission	Low	High
Clock synchronization requirement	nanosecond-level	picosecond-level
Frequency and bandwidth requirement	No specific requirement	Must be identical across all nodes
Usage scenarios	Cooperative Radar/ISAC systems	DACR only
Sensing performance enhancement	Small improvement	Significant improvement

Table 2 – Parameters and values in the paper

Parameter	Symbol	Values
Bandwidth of each BS	B	100 MHz
Subcarrier spacing	Δf	30 KHz
Subcarriers in B	N_c	3333
Sensing signals in B	N_s	101
Comb size in frequency domain	$C_f = \frac{N_c}{N_s}$	33
Comb size in time domain	C_t	7
Symbol duration	T_{sym}	35.67 μs
Number of BS	N_{BS}	5
Phase difference between BS-p and BS-1	$\Delta\phi_{p,1}$	$[0, 2\pi)$
Clock difference between BS-p and BS-1	$\Delta t_{p,1}$	10-50 ns

3. SIGNAL-LEVEL FUSION SYSTEM MODEL

3.1 CA range estimation with perfect clock synchronization

To achieve bandwidth enhancement through CA, a multi-BS scenario is considered where N_{BS} co-located BSs, operated by different operators, share antennas and adjacent frequency bands, each with a bandwidth of B. These BSs simultaneously transmit sensing signals with the same pattern. An example of such a scenario, with five BSs transmitting in the 3.6-4.1 GHz band, is illustrated in Fig. 4. Comb-type sensing signals are transmitted at intervals of C_f subcarriers (comb-C_f) in the frequency domain and every C_t symbols (comb-C_t) in the time domain [17]. The parameters and their respective symbols are summarized in Table 2. Initially, perfect clock synchronization among BSs is assumed. The normalized sensing signal vector $\mathbf{d}_{syn} \in \mathbb{C}^{N_{BS}N_s}$, composed of signals from N_{BS} BSs, with a total bandwidth of $N_{BS}B$, is obtained by element-wise division (Hadamard division) of the receive echo vector $\mathbf{d}_{RX}$ by the transmit signal vector $\mathbf{d}_{TX}$ [18, 19]:

$$d_{syn}(n) = \frac{d_{RX}(n)}{d_{TX}(n)} = e^{-j\frac{4\pi\Delta f R C_f n}{c_0}}, \quad n = 0, \cdots, N_{BS}N_s - 1 \quad (1)$$

where R denotes the distance between the BSs and the target, N_s represents the number of sensing signals within the bandwidth B, and c_0 is the speed of light.

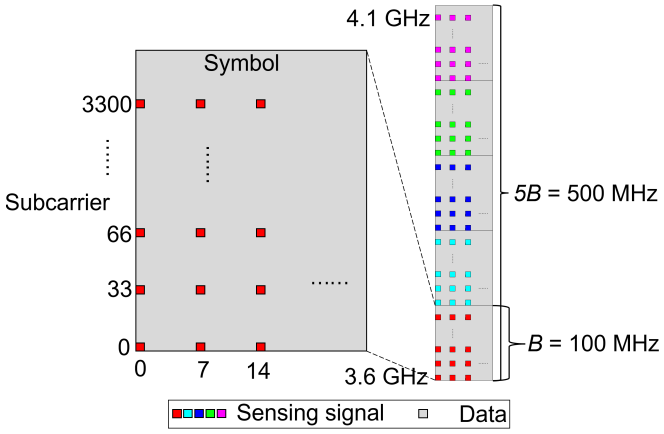

Figure 4 – Comb-type sensing signal pattern across a 500 MHz bandwidth for five operators.

Fig. 5a illustrates an example of the phase variation in the real part of $\mathbf{d}_{syn}$ from five BSs, with signals from each BS distinguished by different colors. As shown, perfect clock synchronization ensures smooth phase transitions across the boundaries of signals from adjacent BSs. Applying the Inverse Fast Fourier Transform (IFFT) to $\mathbf{d}_{syn}$ generates the range profile:

$$Y_{syn}(k) = \mathrm{IFFT}(d_{syn}(n)) = \frac{1}{N_{BS}N_s} \sum_{n=0}^{N_{BS}N_s-1} e^{-j\frac{4\pi\Delta f R C_f n}{c_0}} e^{j\frac{2\pi nk}{N_{BS}N_s}}, \quad k = 0, \cdots, N_{BS}N_s - 1 \quad (2)$$

A peak appears at bin index $k_{\text{peak}} = \frac{2\Delta f R N_{\text{BS}} N_{\text{c}}}{c_0}$ in the plot of $Y_{\text{syn}}(k)$, enabling the estimation of the range R as:

$$R = \frac{c_0 k_{\text{peak}}}{2\Delta f N_{\text{BS}} N_{\text{c}}}. \quad (3)$$

3.2 CA range estimation with clock synchronization error

Although all sensing signals within a single BS are internally synchronized, perfect synchronization between BSs is unattainable, resulting in constant phase offset relative to other BSs. Using the phase of signals from BS-1 as the base phase, $\Delta\phi_{p,1}$ denotes the phase difference between BS-p and BS-1, induced by clock synchronization errors. The combined echo signal vector $\mathbf{d}_{\text{unsyn}} \in \mathbb{C}^{N_{\text{BS}}N_{\text{s}}}$, composed of signals from N_{BS} BSs, is expressed as:

$$d_{\text{unsyn}}(n) = \mathrm{e}^{-\mathrm{j}\left(\frac{4\pi\Delta f R C_{\text{f}} n}{c_0} + \Delta\phi_{\lfloor \frac{n}{N_{\text{s}}} \rfloor + 1,1}\right)},\ n = 0, \cdots, N_{\text{BS}}N_{\text{s}} - 1 \quad (4)$$

In *(4)*, the phase difference relative to BS-1, $\Delta\phi_{\lfloor \frac{n}{N_{\text{s}}} \rfloor + 1,1}$, is indexed by $\left\lfloor \frac{n}{N_{\text{s}}} \right\rfloor + 1$, where $\lfloor \cdot \rfloor$ is the floor function, mapping each n to the corresponding BS index. This model reflects a practical scenario in which internal synchronization within each BS is perfect, but discrepancies arise between BSs due to inherent synchronization imperfections. For example, Fig. 5b illustrates an example of the phase variation in $\mathbf{d}_{\text{unsyn}}$ for five BSs with random clock offsets, resulting in noticeable phase discontinuities at band boundaries.

The IFFT is applied to $\mathbf{d}_{\text{unsyn}}$ to obtain the range profile:

$$\begin{aligned} Y_{\text{unsyn}}(k) &= \text{IFFT}(d_{\text{unsyn}}(n)) \\ &= \frac{1}{N_{\text{BS}}N_{\text{s}}} \sum_{n=1}^{N_{\text{BS}}N_{\text{S}}-1} \mathrm{e}^{-\mathrm{j}\left(\frac{4\pi\Delta f R C_{\text{f}} n}{c_0} + \Delta\phi_{\lfloor \frac{n}{N_{\text{s}}} \rfloor + 1,1}\right)} \mathrm{e}^{\mathrm{j}\frac{2\pi n k}{N_{\text{BS}}N_{\text{s}}}}, \\ & \qquad k = 0, 1, \cdots, N_{\text{BS}}N_{\text{s}} - 1 \quad (5) \end{aligned}$$

Since the phase error $\Delta\phi_{p,1}$ remains constant for all N_{s} signals from the same BS, p is defined as the BS index, ranging from 1 to N_{BS}, and n_p is defined as the signal index for the p-th BS, where n_p spans from pN_{s} to $(p+1)N_{\text{s}} - 1$. With these two indices, the summation in *(5)* can be reformulated by segmenting it into components corresponding to each BS, as follows:

$$\begin{aligned} Y_{\text{unsyn}}(k) &= \frac{1}{N_{\text{BS}}N_{\text{s}}} \sum_{p=1}^{N_{\text{BS}}} \sum_{n_p = pN_{\text{s}}}^{(p+1)N_{\text{s}}-1} \mathrm{e}^{-\mathrm{j}\left(\frac{4\pi\Delta f R C_{\text{f}} n_p}{c_0} + \Delta\phi_{p+1,1}\right)} \mathrm{e}^{\mathrm{j}\frac{2\pi n_p k}{N_{\text{BS}}N_{\text{s}}}}, \\ & \qquad k = 0, 1, \cdots, N_{\text{BS}}N_{\text{s}} - 1 \quad (6) \end{aligned}$$

To enable a clearer analysis of the impact of synchronization errors, an internal signal index q is redefined within the BS, such that $n_p = pN_{\text{s}} + q$, where $q = 0, 1, ..., N_{\text{s}} - 1$. Substituting this redefinition into *(6)* gives:

$$\begin{aligned} Y_{\text{unsyn}}(k) &= \frac{1}{N_{\text{BS}}N_{\text{s}}} \sum_{p=1}^{N_{\text{BS}}} \sum_{q=0}^{N_{\text{s}}-1} e^{-\mathrm{j}\left(\frac{4\pi\Delta f R C_{\text{f}}(pN_{\text{s}}+q)}{c_0} + \Delta\phi_{p+1,1}\right)} e^{\mathrm{j}\frac{2\pi(pN_{\text{s}}+q)k}{N_{\text{BS}}N_{\text{s}}}}, \\ & \qquad k = 0, 1, \cdots, N_{\text{BS}}N_{\text{s}} - 1 \quad (7) \end{aligned}$$

This redefinition enables a more direct analysis of contributions from different BSs and provides a clearer understanding of how these contributions are aggregated in the range profile. By transforming the expression in *(7)*, the individual contributions are consolidated into a more structured representation:

$$\begin{aligned} & Y_{\text{unsyn}}(k) \\ &= \frac{1}{N_{\text{BS}}N_{\text{s}}} \underbrace{\sum_{p=1}^{N_{\text{BS}}} \overbrace{\mathrm{e}^{-\mathrm{j}\Delta\phi_{p+1,1}}}^{\text{Term 3}} \overbrace{\mathrm{e}^{-\mathrm{j}\frac{4\pi\Delta f R C_{\text{f}} N_{\text{s}} p}{c_0}}}^{\text{Term 1}} \overbrace{\mathrm{e}^{\mathrm{j}\frac{2\pi p k}{N_{\text{BS}}}}}^{\text{Term 2}}}_{Y_1(k)} \underbrace{\sum_{q=0}^{N_{\text{s}}-1} \mathrm{e}^{-\mathrm{j}\frac{4\pi\Delta f R C_{\text{f}} q}{c_0}} \mathrm{e}^{\mathrm{j}\frac{2\pi q k}{N_{\text{BS}}N_{\text{s}}}}}_{Y_2(k)}, \\ & \qquad k = 0, \cdots, N_{\text{BS}}N_{\text{s}} - 1 \quad (8) \end{aligned}$$

Equation *(8)* denotes that vector $\mathbf{Y}_{\text{unsyn}}$ is the Hadamard product of each element in vector $\mathbf{Y_1} \in \mathbb{C}^{N_{\text{BS}}N_{\text{s}}}$ and vector $\mathbf{Y_2} \in \mathbb{C}^{N_{\text{BS}}N_{\text{s}}}$, i.e.,

$$\mathbf{Y}_{\text{unsyn}} = \frac{1}{N_{\text{BS}}N_{\text{s}}} \mathbf{Y_1} \odot \mathbf{Y_2}. \quad (9)$$

Terms 1 and 2 in *(8)* cancel each other, resulting in unity under the condition:

$$\frac{4\pi\Delta f R C_{\text{f}} N_{\text{s}} p}{c_0} = \frac{2\pi p k}{N_{\text{BS}}}. \quad (10)$$

This indicates that a peak appears at the bin index $\frac{2\Delta f R N_{\text{BS}} N_{\text{c}}}{c_0}$ in the plot of $\mathbf{Y_1}$. Term 2 repeats every N_{BS} bins, resulting in a periodic structure in the plot of $\mathbf{Y_1}$. Consequently, additional peaks appear at bin indices $\frac{2\Delta f R N_{\text{BS}} N_{\text{c}}}{c_0} \pm N_{\text{BS}}$, $\frac{2\Delta f R N_{\text{BS}} N_{\text{c}}}{c_0} \pm 2N_{\text{BS}}$, and so on. Thus, the plot of $\mathbf{Y_1}$ exhibits a comb-like distribution of peaks, with adjacent peaks separated by N_{BS} bins. Random phase shifts in term 3 cause the amplitudes of these peaks to vary with bin position.

For $\mathbf{Y_2}$, when $k = 0, N_{\text{BS}}, \cdots, N_{\text{s}}N_{\text{BS}}$, $Y_2(k)$ corresponds to the N_{s}-point IFFT to $\mathrm{e}^{-\mathrm{j}\frac{4\pi\Delta f R C_{\text{f}} q}{c_0}}$, representing a range profile derived from a bandwidth B containing N_{s} sensing signals. For other values of k, $N_{\text{BS}} - 1$ additional bins are interpolated between each pair of adjacent bins in the radar profile. This interpolation increases the number of bins from N_{s} to $N_{\text{s}}N_{\text{BS}}$, effectively stretching the range

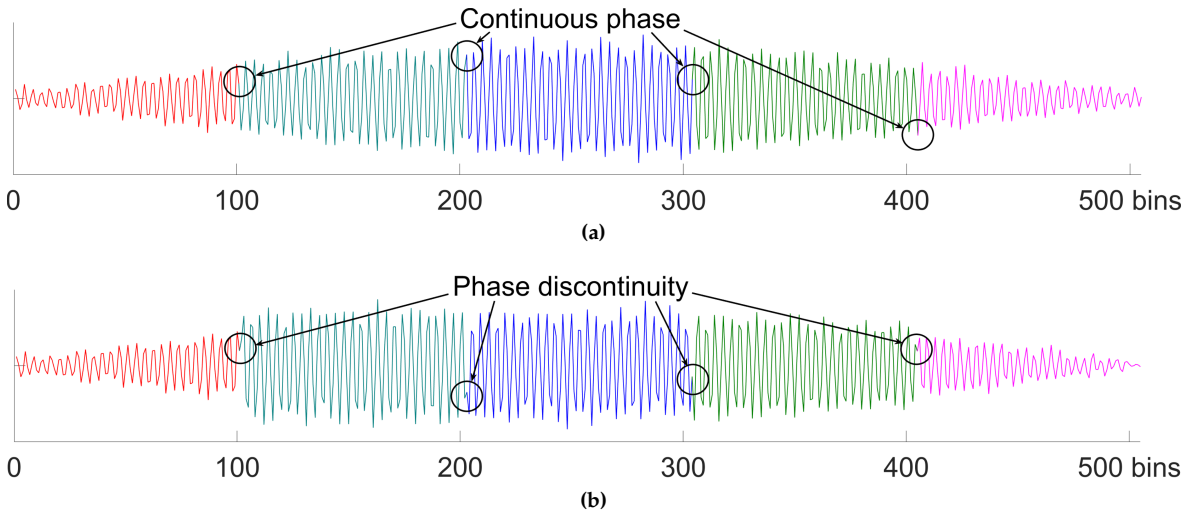

Figure 5 – Phase variation in concatenated echo signals. (a) With perfect clock synchronization. (b) With clock synchronization errors.

profile horizontally. However, it does not enhance range resolution, as the resolution is solely determined by the bandwidth B owned by a single BS.

Compared to the case of perfect clock synchronization, the range profile described by *(9)* exhibits two notable characteristics caused by clock synchronization errors between BSs. First, the range resolution is degraded by a factor of N_{BS}, resulting in broadened peaks induced by targets. This degradation is attributed to interpolations in $\mathbf{Y_2}$. Second, the range profile displays a phenomenon termed the "fishbone effect," characterized by a comb-like structure with peaks spaced N_{BS} bins apart, arising from the periodicity introduced by $\mathbf{Y_1}$.

3.3 CA range estimation for multi-target scenarios

The above analysis primarily considers a single-target scenario. However, the proposed method is also applicable to multi-target scenarios. For a multi-target scenario with N_{T} targets, *(8)* is modified as:

$$Y_{\mathrm{unsyn}}(k) = \frac{1}{N_{\mathrm{BS}}N_{\mathrm{s}}} \underbrace{\sum_{p=1}^{N_{\mathrm{BS}}} \mathrm{e}^{-\mathrm{j}\Delta\phi_{p,1}} \sum_{i=1}^{N_{\mathrm{T}}} \mathrm{e}^{-\mathrm{j}\frac{4\pi\Delta f R_i C_{\mathrm{f}} N_{\mathrm{s}} p}{c_0}} \mathrm{e}^{\mathrm{j}\frac{2\pi pk}{N_{\mathrm{BS}}}}}_{Y_1(k)} \times \underbrace{\sum_{q=0}^{N_{\mathrm{s}}-1} \sum_{i=1}^{N_{\mathrm{T}}} \mathrm{e}^{-\mathrm{j}\frac{4\pi\Delta f R_i C_{\mathrm{f}} q}{c_0}} \mathrm{e}^{\mathrm{j}\frac{2\pi qk}{N_{\mathrm{BS}}N_{\mathrm{s}}}}}_{Y_2(k)},$$
$$k = 0, \cdots, N_{\mathrm{BS}}N_{\mathrm{s}} - 1 \quad (11)$$

Similarly as the analysis for single-target scenarios, in multi-target scenarios, for the i-th target, a peak appears at the bin index $\frac{2\Delta f R_i N_{\mathrm{BS}} N_{\mathrm{c}}}{c_0}$ in the plot of $\mathbf{Y_1}$, and due to periodicity, it presents a series of comb-like peaks with a comb size equal to N_{BS}. The N_{T} targets will cause the superposition of N_{T} comb-like patterns, resulting in a range profile with numerous interlaced peaks. This severely affects both range resolution and range accuracy.

4. MITIGATING PHASE DISCONTINUITIES WITH SUBSEQUENT ECHO SIGNALS

4.1 The proposed method

To address phase discontinuities caused by imperfect clock synchronization in multi-BS CA scenarios, a method is proposed that utilizes subsequent echo signals to identify and align segments with improved phase continuity. By exploiting the periodicity of sensing signals, this approach progressively reduces or eliminates phase discontinuities at the boundaries between signals from different BSs.

First, assuming perfect clock synchronization between two BSs, Fig. 6a illustrates the phase variations across the band boundary between the two BSs. To clearly demonstrate the phase transitions, Fig. 6a only shows a limited set of echo signals received by both BSs. The red curves represent the real part of the time-domain echoes from BS-1, while the cyan curves correspond to those from BS-2. The black circle markers at time t_0 indicate the phase of each echo signal at that moment. Due to the perfect synchronization between the BSs, the phase transitions (represented by the black dashed line connecting the markers) are smooth across the boundary.

In practice, clock errors typically exist between BSs. To illustrate the proposed method, Fig. 6b depicts the phase variations at the band boundary between two BSs, BS-1

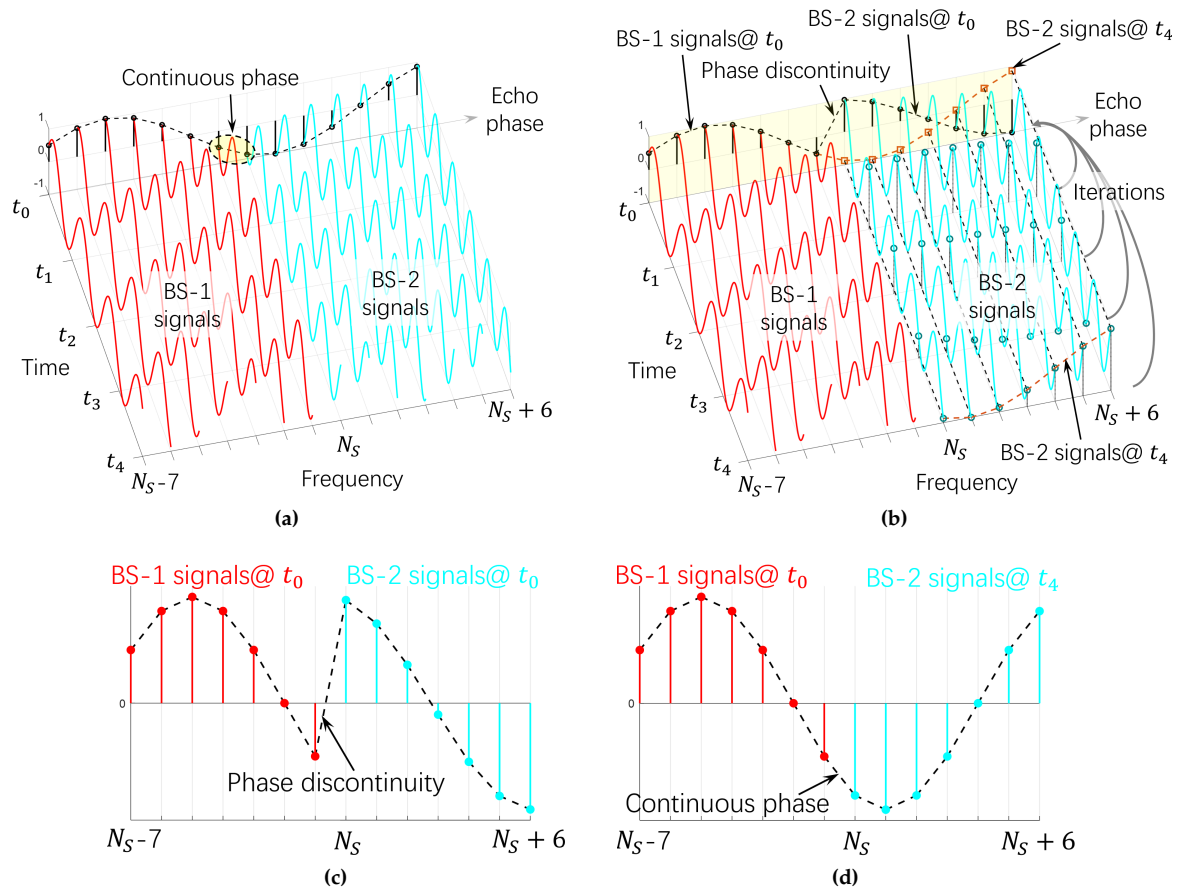

Figure 6 – Phase variation at the BS band boundary. (a) Phase variation with perfect clock synchronization. (b) Phase variation with clock synchronization errors. (c) Phase discontinuity at t_0. (d) Phase alignment after applying the proposed method.

and BS-2 with clock synchronization errors. When the echo signals received from BS-1 and BS-2 at time t_0 are concatenated, a noticeable phase discontinuity caused by clock synchronization errors is evident at the band boundary. This phase discontinuity is more clearly visualized in Fig. 6c.

The proposed method mitigates this phase discontinuity by progressively concatenating the BS-1 echo signals received at t_0 with the BS-2 echo signals received at subsequent time instances, and checking whether the fishbone effect persists. This iterative process continues until phase discontinuity is eliminated. In the example shown in Fig. 6b, after concatenating the echo signals received at time $t_4 = 4C_tT_{sym}$, the phase of the BS-2 echo signals (represented as brown dashed lines and square markers in Fig. 6b) aligns seamlessly with that of the BS-1 signals. Fig. 6d provides a clearer visualization of the achieved phase continuity after concatenation, demonstrating the effectiveness of the proposed method in resolving the phase discontinuity.

The clock error between BS-p and BS-1 is defined as $\Delta t_{p,1}$. The echo signal received by BS-p at time t_0 is modeled as:

$$d_{\text{unsyn},p,t_0}(n) = \mathrm{e}^{-\mathrm{j}\left(\frac{4\pi\Delta f R C_f n}{c_0} + \Delta\phi_{p,1} n\right)},\ n = (p-1)N_\mathrm{s}, \ldots, pN_\mathrm{s} - 1 \quad (12)$$

where $\Delta\phi_{p,1} = 4\pi\Delta f \Delta t_{p,1} C_\mathrm{f}$ denotes the phase discontinuity caused by the clock error.

For each subsequent echo signal from BS-p, the time difference between consecutive signals is C_tT_{sym}, which introduces an additional phase shift of $4\pi\Delta f C_t T_{sym} C_f$, denoted by $\Delta\phi_{step}$. Therefore, the echo signal received by BS-p at time t_m is expressed as:

$$d_{\text{unsyn},p,t_m}(n) = \mathrm{e}^{-\mathrm{j}\left(\frac{4\pi\Delta f R C_f n}{c_0} + \Delta\phi_{p,1} n + m\cdot\Delta\phi_{\text{step}} n\right)},$$
$$m = 1, 2, 3, \cdots;\ n = (p-1)N_\mathrm{s}, \cdots, pN_\mathrm{s} - 1 \quad (13)$$

It is assumed that the phase is considered continuous when the phase difference becomes smaller than a predefined threshold $\Delta\phi_{\text{thresh}}$ (e.g., 0.01π radians); this condition requires finding m such that:

$$\left|\Delta\phi_{p,1} + m\cdot\Delta\phi_{\text{step}}\right| < \Delta\phi_{\text{thresh}},\ m = 1, 2, 3, \cdots \quad (14)$$

However, directly searching for m that satisfies *(14)* can

be extremely time-consuming. To overcome this, the aim is instead to find m such that

$$\left|\Delta\phi_{p,1} + m \cdot \Delta\phi_{\text{step}}\right| \mod 2\pi < \Delta\phi_{\text{thresh}},\ m = 1, 2, 3, \cdots \tag{15}$$

The echo signals at different times t_m are iteratively concatenated until condition *(15)* is satisfied for a small $\Delta\phi_{\text{thresh}}$, e.g., 0.01π radians. The success of this process can be verified by observing whether the fishbone effect has been effectively eliminated. Once this is achieved, the concatenated signals are suitable for generating a more accurate range profile.

The proposed method is summarized in Algorithm 1.

Algorithm 1 Mitigating phase discontinuities

Initialize parameters: $\Delta\phi_{\text{thresh}}$, C_t, N_s
Set $m = 0$ ▷ Iteration counter
Obtain echo signals d_{unsyn,p,t_0} from BS-p at time t_0
repeat
  Calculate phase discontinuity: $\Delta\phi_{p,1} = \text{Phase}(d_{\text{unsyn},p,t_0})$
  if $|\Delta\phi_{p,1}| < \Delta\phi_{\text{thresh}}$ **then** ▷ Check for phase continuity
    Break ▷ Phase continuity achieved
  end if
  Update time: $t_m = t_0 + m \cdot C_t T_{\text{sym}}$
  Retrieve echo signals d_{unsyn,p,t_m} from BS-p at t_m
  Concatenate echo signals: $d_{\text{concat}} = d_{\text{unsyn},p,t_0} + d_{\text{unsyn},p,t_m}$
  Increment m: $m = m + 1$
until Maximum iterations reached
if Phase continuity not achieved **then**
  Output: "Phase discontinuity persists"
else
  Output: "Phase continuity established"
end if

Fig. 7 illustrates an example of the phase change process during multiple replacements. The black spiral represents the phase evolution of BS-p with each replacement, while the red line indicates the phase of BS-1 at time t_0. The red sector represents the acceptable phase range $\pm\Delta\phi_{\text{thresh}}$ (where $\Delta\phi_{\text{thresh}} = 0.01\pi$ (1.8°)) around the phase of BS-1 at time t_0. Each replacement introduces a phase change of approximately 1.706π (307°), which is determined by the clock error between BS-1 and BS-p, as shown by the green arc in Fig. 7. The process continues until the phase of BS-p falls within the red sector, signaling a successful match. The number of replacements varies depending on the initial random phase value of BS-1 at time t_0 and the clock error between BS-1 and BS-p.

The implementation of the proposed method in practical systems requires consideration of various aspects. To reduce overall processing delay and sensing signal overhead, the symbol positions of sensing signals from two BSs in a BS pair should be mutually negotiated and

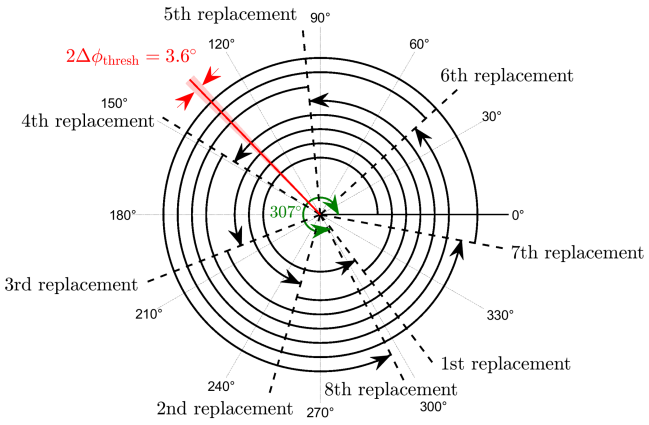

Figure 7 – Proposed replacement algorithm: phase change process and matching criteria.

reasonably configured, aiming to achieve as many phase differences between sensing signals as possible with minimal sensing signals. Additionally, the phase matching process between different BS pairs can be executed in parallel. Although a fixed threshold is used in the algorithm, an adaptive threshold based on signal-to-noise ratio can further enhance performance under varying channel conditions. The algorithm can be terminated early if a sufficiently good match is found, even if not optimal, balancing the trade-off between accuracy and delay. These implementation considerations ensure that the algorithm remains suitable for real-time applications while maintaining its effectiveness in mitigating phase discontinuities.

4.2 Phase matching and delay analysis

The proposed algorithm requires multiple iterations to achieve phase continuity, which inevitably introduces a delay in obtaining range estimations. In *(15)*, $\Delta\phi_{p,1}$ represents the initial phase discontinuity, uniformly distributed in $[0, 2\pi)$, while $\Delta\phi_{\text{step}}$ denotes the phase shift introduced with each concatenation, also uniformly distributed in $[0, 2\pi)$. The goal is to bring the cumulative phase into a small target window of width $2\Delta\phi_{\text{thresh}}$, to ensure phase continuity.

This phase matching problem can be modeled as a random walk on a circle of 2π [20]. For each concatenation, the probability of the cumulative phase falling within the target window is proportional to the ratio of the target window's width, $2\Delta\phi_{\text{thresh}}$, to the total circumference, 2π. Accordingly, the expected number of concatenations, $E[m]$, required to achieve phase continuity is given by:

$$E[m] = \frac{\pi}{\Delta\phi_{\text{thresh}}}. \tag{16}$$

For example, if $\Delta\phi_{\text{thresh}} = 0.01\pi$, the expected number of concatenations is approximately 100. Thus, the delay introduced by the algorithm depends on both the de-

sired phase precision and the time-domain sensing signal density, C_t. While reducing $\Delta\phi_{\text{thresh}}$ improves accuracy, it also increases the delay, requiring a careful trade-off between precision and efficiency.

It is important to note that, when extending the method to multiple BS pairs, the phase matching delay increases multiplicatively, as each pair must independently achieve its phase matching. Therefore, the method is particularly suited for specific scenarios where high-precision ranging is critical while targets are either stationary or moving at low speeds, such as indoor positioning, environmental reconstruction, or industrial monitoring applications.

5. SIMULATION RESULTS AND PERFORMANCE EVALUATION

In this section, the performance of the proposed method is evaluated through simulations. Two primary performance metrics are employed: range accuracy and location accuracy. Range accuracy is defined as the absolute difference between the estimated range and the actual range of the target: $\varepsilon_R = |R_{estimated} - R_{actual}|$. This metric directly quantifies the precision of the range estimation. Location accuracy is defined as the Euclidean distance between the estimated position and the actual position of the target: $\varepsilon_L = \sqrt{(x_{estimated} - x_{actual})^2 + (y_{estimated} - y_{actual})^2}$. These metrics allow for objective comparison across different methods and scenarios, evaluating both the direct sensing performance and the derived positioning capability of our system.

5.1 Validation of theoretical analysis

The proposed algorithm is validated through simulations in a multi-target scenario. The simulations use the spectrum allocation shown in Fig. 1, with parameters listed in Table 2. Two targets, labeled as target-1 and target-2, are located at distances $R_1 = 40$ m and $R_2 = 80$ m from the BS, respectively. As shown in Fig. 8a, the range profile obtained with a 100 MHz bandwidth reveals two peaks at bin 27 (40.5 m) and bin 53 (79.5 m). The range errors of 0.5 m, coupled with the broad peak shapes, underscore the limitations of using a narrow 100 MHz bandwidth. After applying CA to extend the bandwidth to 500 MHz and assuming perfect clock synchronization among BSs, the resulting range profile, shown in Fig. 8b, exhibits two much sharper peaks at bin 133 (39.9 m) and bin 267 (80.1 m). The small range errors highlight a significant improvement compared to the 100 MHz bandwidth scenario.

In practice, achieving perfect synchronization between BSs is not feasible. In our simulations, random clock errors of 10 to 50 ns are introduced between the BSs. The resulting range profile is shown in Fig. 8c. Despite using a 500 MHz bandwidth, the peak widths in Fig. 8c are significantly broader than those in Fig. 8b, and are similar in width to those observed in Fig. 8a. As analyzed in Section 3, the interpolation from N_s to $N_s N_{BS}$ bins in vector $\mathbf{Y_2}$ does not improve the resolution. In other words, the interpolation fails to sharpen the peaks, indicating that clock synchronization errors negate the benefits of bandwidth aggregation.

To better illustrate the fishbone effect observed in Fig. 8c, Fig. 9a provides a zoomed-in view of the yellow-highlighted region (bin 120-180) in Fig. 8c. As analyzed in Section 3, the range profile in Fig. 9a is the Hadamard product of the vectors $Y_1(k)$ and $Y_2(k)$, as described in *(11)*. Fig. 9b shows the plot of $Y_1(k)$, where target-1 generates a series of peaks marked by red markers, and target-2 corresponds to the peaks marked by green markers. The spacing between adjacent red (or green) peaks is 5 bins, consistent with the analysis of the fishbone effect in Section 3. The random phase errors $\Delta\phi_{p,1}$ affect both the amplitudes and positions of these peaks. Fig. 9c presents the plot of $Y_2(k)$, derived from the range profile in the yellow-highlighted region of Fig. 8a after interpolation. The combined influence of $Y_1(k)$ and $Y_2(k)$ through the Hadamard product explains the fishbone effect and the broad peaks observed in Fig. 9a. Fig. 8d presents the range profile obtained after applying the proposed method with $\Delta\phi_{\text{thresh}} = 0.01\pi$, where the fishbone effect has been largely eliminated. Compared to Fig. 8c, the peaks corresponding to the targets are significantly sharper and more distinct, demonstrating a notable improvement in range resolution and accuracy. For instance, in Fig. 8c and Fig. 8d, the peak corresponding to target-1 is located at bin 135 (40.5 m) and bin 133 (39.9 m), respectively. The proposed method reduces the range error from 0.5 m to 0.1 m, highlighting its effectiveness in mitigating phase discontinuities. While the range profile in Fig. 8d remains slightly inferior to the ideal case with perfect synchronization, as shown in Fig. 8b, this discrepancy arises from residual phase discontinuities that were not fully corrected. Nevertheless, the proposed method effectively minimizes the impact of these discontinuities, resulting in a range profile that closely approximates the performance of an ideal 500 MHz bandwidth system.

5.2 Comprehensive performance evaluation

To thoroughly evaluate the performance of our proposed method in realistic scenarios, extensive simulations involving multi-BS ranging and positioning are conducted. The simulation setup is illustrated in Fig. 10, where for the perfect clock synchronization scenario, one BS is located at (0,0) and another BS at (50,0), while for the CA with clock error scenario, two BSs are located at (0,0) and another two BSs are located at (50,0). One hundred

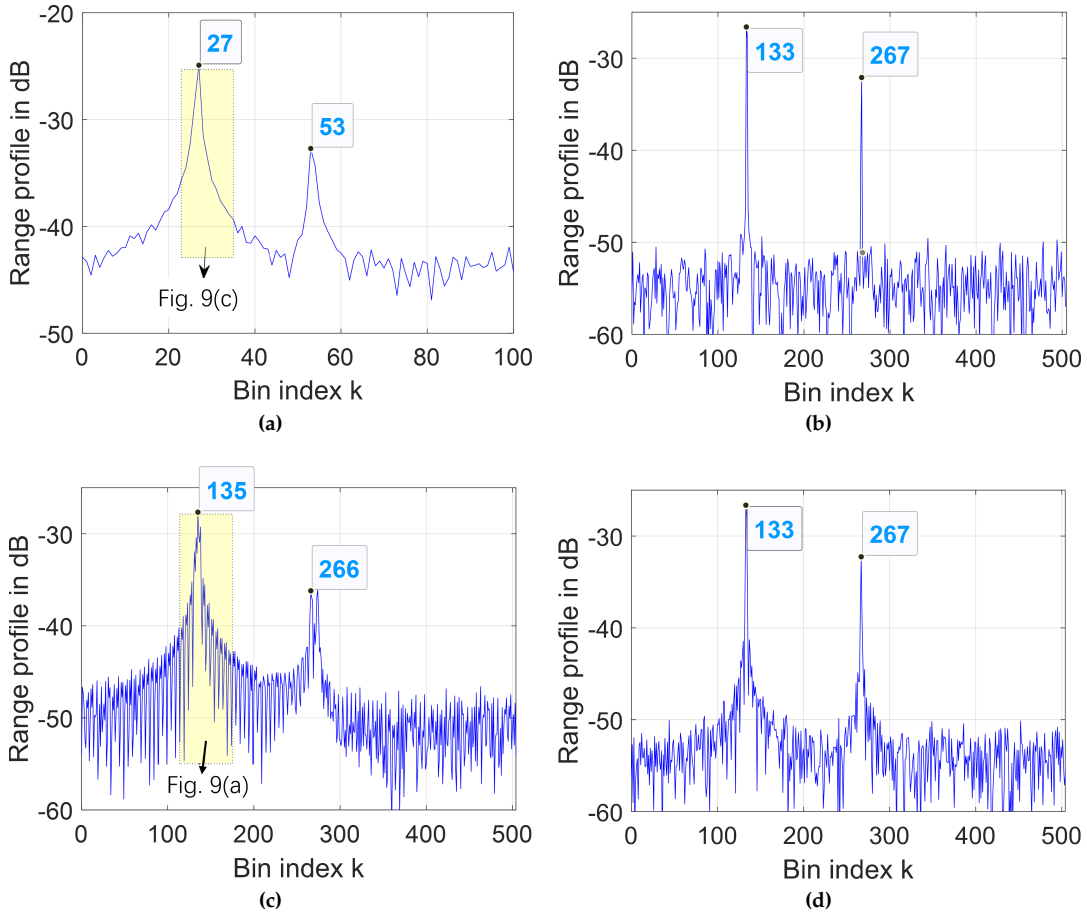

Figure 8 – Range profiles under different bandwidths and clock synchronization conditions. (a) From a single BS with 100 MHz bandwidth. (b) From five BSs with perfect synchronization (500 MHz bandwidth). (c) From five BSs with imperfect synchronization (500 MHz bandwidth). (d) Using the proposed method (500 MHz bandwidth).

targets within a square area bounded by coordinates (0, 0), (50, 0), (0, 50), and (50, 50) are randomly distributed.

Fig. 10 depicts the simulation scenario, where blue dots represent the actual target positions, and magenta dots indicate the estimated positions calculated through triangulation based on range measurements from BSs at (0,0) and (50,0). This positioning approach leverages the geometric relationship between the BSs and their respective distance measurements to determine the target's coordinates.

In our evaluation framework, three distinct configurations are compared:

- Single-BS with 100 MHz bandwidth under perfect clock synchronization;
- Single-BS with 200 MHz bandwidth under perfect clock synchronization;
- Two BSs each with 100 MHz bandwidth using our proposed method under clock synchronization errors.

Fig. 11a presents the Cumulative Distribution Function (CDF) of range accuracy for these three configurations. The blue curve represents the 100 MHz bandwidth case with perfect synchronization, the green curve shows the 200 MHz bandwidth case with perfect synchronization, and the red curve illustrates the performance of our proposed method with two 100 MHz bandwidth BSs under clock synchronization errors. The results demonstrate that at CDF = 0.9, the range errors are 0.93 m, 0.44 m, and 0.50 m for the three configurations, respectively.

Similarly, Fig. 11b displays the CDF of location accuracy. At CDF = 0.9, the location errors are 1.34 m, 0.55 m, and 0.64 m for the three configurations. These results reveal that the proposed method significantly outperforms the single 100 MHz bandwidth system and achieves performance very close to that of the 200 MHz bandwidth system with perfect synchronization.

The superior performance of our method can be attributed to its effective mitigation of phase discontinuities between signals from different BSs. By leveraging subsequent echo signals and applying the phase matching algorithm described in Section 4, a 200 MHz bandwidth system is effectively created from two 100 MHz BSs, despite the presence of clock synchronization errors.

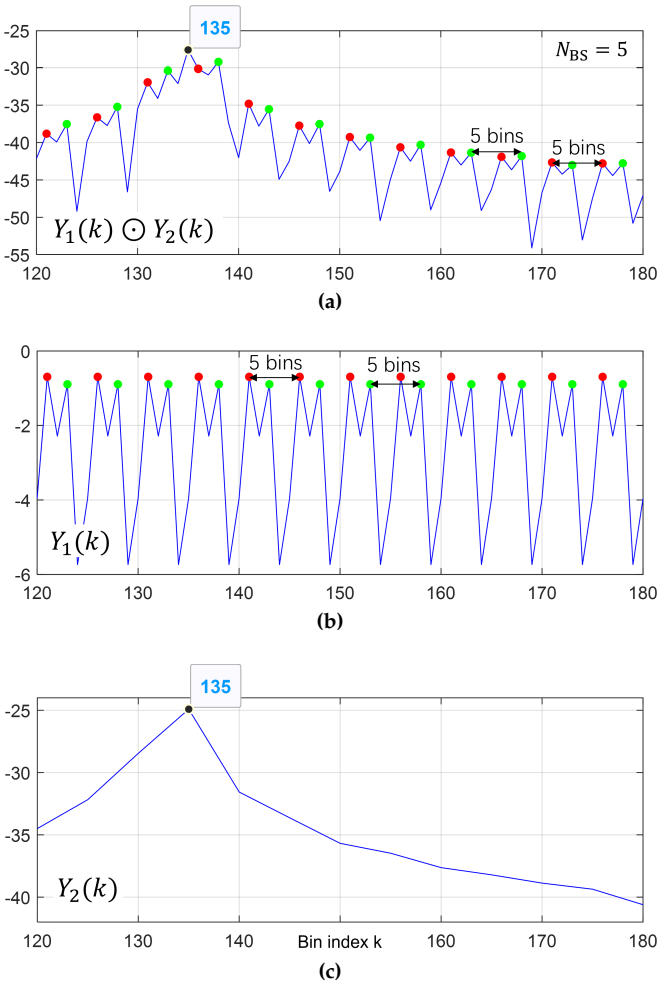

Figure 9 – Illustration of the fishbone effect. (a) Range profile containing fishbone effect. (b) $Y_1(k)$. (c) $Y_2(k)$.

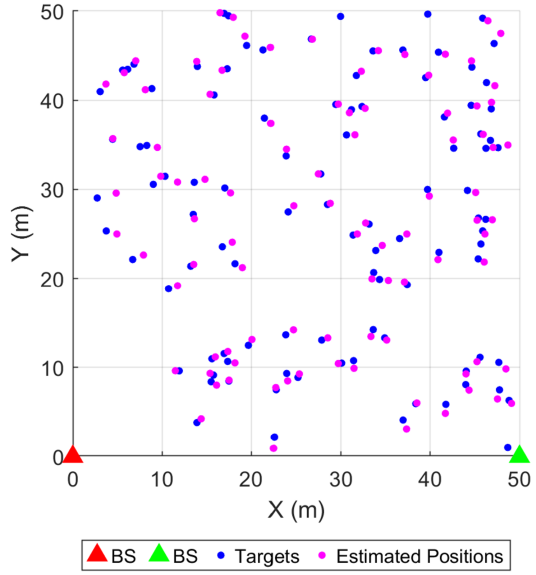

Figure 10 – Simulation scenario with multiple targets.

It is worth noting that the slight performance gap between our proposed method and the ideal 200 MHz bandwidth system (0.50 m vs. 0.44 m for range accuracy and 0.64 m vs. 0.55 m for location accuracy) stems from residual phase discrepancies that could not be completely eliminated. Nevertheless, the results conclusively demonstrate that our proposed phase-continuous method effectively enables cross-operator CA for high-precision ranging and positioning in practical ISAC systems where perfect synchronization between BSs is unattainable.

6. CONCLUSION

This paper presents a novel method for high-precision ranging in ISAC systems operating across fragmented low-frequency bands. By leveraging successive echo signals, the proposed method effectively mitigates phase discontinuities caused by clock synchronization errors between BSs, significantly reducing the fishbone effect and enhancing range resolution. Simulation results confirm that the proposed approach produces sharper peaks in range profiles, closely approximating the performance of ideal synchronized systems. This work offers a practical solution for achieving high-precision ranging in 6G ISAC systems and establishes a foundation for further research in real-world applications.

ACKNOWLEDGEMENT

This work has been funded by the National Key R&D Program of China (SQ2024YFE0200406).

REFERENCES

[1] Nuria González-Prelcic, Musa Furkan Keskin, Ossi Kaltiokallio, Mikko Valkama, Davide Dardari, Xiao Shen, Yuan Shen, Murat Bayraktar, and Henk Wymeersch. "The Integrated Sensing and Communication Revolution for 6G: Vision, Techniques, and Applications". In: *Proceedings of the IEEE* (2024), pp. 1–. DOI: 10.1109/JPROC.2024.3397609.

[2] Victor Shatov, Benjamin Nuss, Steffen Schieler, Pradyumna Kumar Bishoyi, Lara Wimmer, Maximilian Lübke, Navid Keshtiarast, Christoph Fischer, Daniel Lindenschmitt, Benedikt Geiger, Reiner Thomä, Amina Fellan, Laurent Schmalen, Marina Petrova, Hans D. Schotten, and Norman Franchi. "Joint Radar and Communications: Architectures, Use Cases, Aspects of Radio Access, Signal Processing, and Hardware". In: *IEEE Access* 12 (2024), pp. 47888–47914. DOI: 10.1109/ACCESS.2024.3383771.

[3] Henk Wymeersch, Sharief Saleh, Ahmad Nimr, Rreze Halili, Rafael Berkvens, Mohammad H. Moghaddam, José Miguel Mateos-Ramos, Athanasios Stavridis, Stefan Wänstedt, Sokratis Barmpounakis, Basuki Priyanto, Martin Beale, Jaap van de Beek, Zi Ye, Marvin Manalastas, Apostolos Kousaridas, and Gerhard P. Fettweis. "Joint Communication and Sensing for 6G - A Cross-Layer Perspective". In: *2024 IEEE 4th International Symposium on Joint Communications & Sensing (JC&S)*. 2024, pp. 01–06. DOI: 10.1109/JCS61227.2024.10646326.

[4] Ali Behravan, Vijaya Yajnanarayana, Musa Furkan Keskin, Hui Chen, Deep Shrestha, Traian E. Abrudan, Tommy Svensson, Kim Schindhelm, Andreas Wolfgang, Simon Lindberg, and Henk Wymeersch. "Positioning and Sensing in 6G: Gaps, Challenges, and Opportunities". In: *IEEE Vehicular Technology Magazine* 18.1 (2023), pp. 40–48. DOI: 10.1109/MVT.2022.3219999.

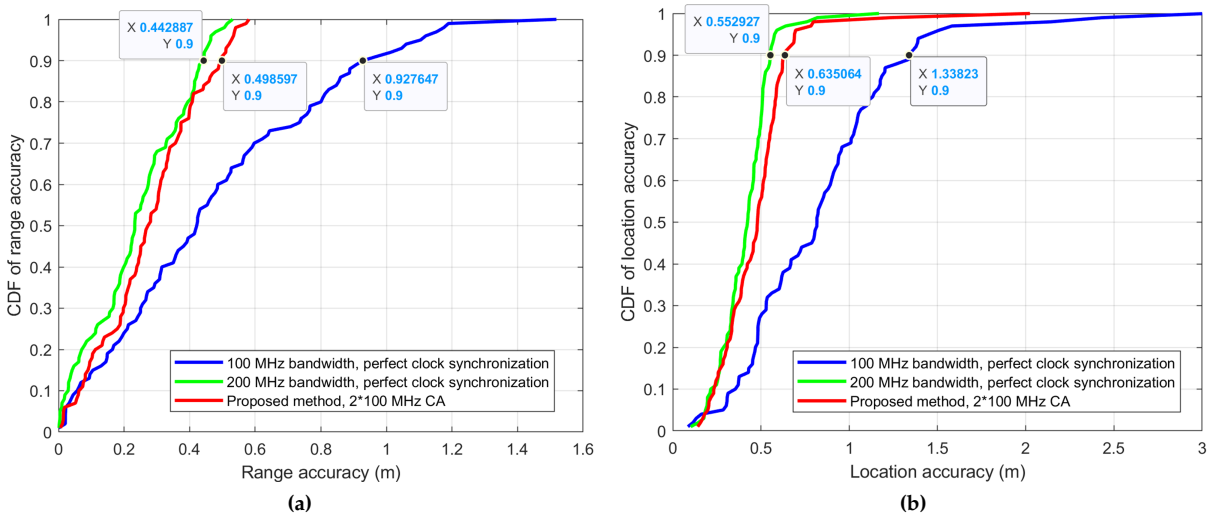

Figure 11 – CDF performance comparison of different configurations. (a) CDF of range accuracy. (b) CDF of location accuracy.

[5] Theodore S. Rappaport, Yunchou Xing, Ojas Kanhere, Shihao Ju, Arjuna Madanayake, Soumyajit Mandal, Ahmed Alkhateeb, and Georgios C. Trichopoulos. "Wireless Communications and Applications Above 100 GHz: Opportunities and Challenges for 6G and Beyond". In: *IEEE Access* 7 (2019), pp. 78729–78757. DOI: 10.1109/ACCESS.2019.2921522.

[6] Josep M. Jornet, Vitaly Petrov, Hua Wang, Zoya Popović, Dipankar Shakya, Jose V. Siles, and Theodore S. Rappaport. "The Evolution of Applications, Hardware Design, and Channel Modeling for Terahertz (THz) Band Communications and Sensing: Ready for 6G?" In: *Proceedings of the IEEE* (2024), pp. 1–32. DOI: 10.1109/JPROC.2024.3412828.

[7] Zhiqing Wei, Haotian Liu, Xinyi Yang, Wangjun Jiang, Huici Wu, Xingwang Li, and Zhiyong Feng. "Carrier Aggregation Enabled Integrated Sensing and Communication Signal Design and Processing". In: *IEEE Transactions on Vehicular Technology* 73.3 (2024), pp. 3580–3596. DOI: 10.1109/TVT.2023.3324436.

[8] Daniel Chew, Andrew L. Adams, and Jason Uher. "LTE Carrier Aggregation and Unlicensed Access". In: *Wireless Coexistence: Standards, Challenges, and Intelligent Solutions*. 2021, pp. 257–279. DOI: 10.1002/9781119584230.ch9.

[9] 3GPP. *Feasibility study for Further Advancement for E-UTRA (LTE-Advanced)*. Technical Report TR 36.912. Version 18.0.0. Release 18. 3rd Generation Partnership Project (3GPP), Mar. 2024.

[10] Kaitao Meng, Christos Masouros, Athina P. Petropulu, and Lajos Hanzo. "Cooperative ISAC Networks: Opportunities and Challenges". In: *IEEE Wireless Communications* (2024), pp. 1–8. DOI: 10.1109/MWC.008.2400151.

[11] Jiahui Zhang, Ziyun Chao, Fanghao Xia, Xinyi Wang, Jingxuan Huang, and Zesong Fei. "Range and Velocity Estimation in Carrier-Aggregation OFDM ISAC Systems". In: *2024 IEEE International Conference on Signal, Information and Data Processing (ICSIDP)*. 2024, pp. 1–5. DOI: 10.1109/ICSIDP62679.2024.10868769.

[12] Benedikt Schweizer, Christina Knill, Daniel Schindler, and Christian Waldschmidt. "Stepped-Carrier OFDM-Radar Processing Scheme to Retrieve High-Resolution Range-Velocity Profile at Low Sampling Rate". In: *IEEE Transactions on Microwave Theory and Techniques* 66.3 (2018), pp. 1610–1618. DOI: 10.1109/TMTT.2017.2751463.

[13] Lei Xie, Shenghui Song, Yonina C. Eldar, and Khaled B. Letaief. "Collaborative Sensing in Perceptive Mobile Networks: Opportunities and Challenges". In: *IEEE Wireless Communications* 30.1 (2023), pp. 16–23. DOI: 10.1109/MWC.005.2200214.

[14] Zhiqing Wei, Wangjun Jiang, Zhiyong Feng, Huici Wu, Ning Zhang, Kaifeng Han, Ruizhong Xu, and Ping Zhang. "Integrated Sensing and Communication Enabled Multiple Base Stations Cooperative Sensing Towards 6G". In: *IEEE Network* 38.4 (2024), pp. 207–215. DOI: 10.1109/MNET.2023.3321690.

[15] Zhiqing Wei, Ruizhong Xu, Zhiyong Feng, Huici Wu, Ning Zhang, Wangjun Jiang, and Xiaoyu Yang. "Symbol-Level Integrated Sensing and Communication Enabled Multiple Base Stations Cooperative Sensing". In: *IEEE Transactions on Vehicular Technology* 73.1 (2024), pp. 724–738. DOI: 10.1109/TVT.2023.3304856.

[16] Hongwei Gao, Baoliang Zhou, Dongming Zhou, and Zhen Jin. "Performance analysis and experimental study on distributed aperture coherence-synthetic radar". In: *2016 CIE International Conference on Radar (RADAR)*. 2016, pp. 1–5. DOI: 10.1109/RADAR.2016.8059191.

[17] Christian Sturm, Martin Braun, and Zwick Thomas. "Spectrally interleaved multi-carrier signals for radar network applications and multi-input multi-output radar". In: *IET Radar, Sonar and Navigation* 7.3 (2012), pp. 261–269. DOI: 10.1049/iet-rsn.2012.0040.

[18] C. Sturm, E. Pancera, T. Zwick, and W. Wiesbeck. "A novel approach to OFDM radar processing". In: *2009 IEEE Radar Conference*. 2009, pp. 1–4. DOI: 10.1109/RADAR.2009.4977002.

[19] Christian Sturm and Werner Wiesbeck. "Waveform Design and Signal Processing Aspects for Fusion of Wireless Communications and Radar Sensing". In: *Proceedings of the IEEE* 99.7 (2011), pp. 1236–1259. DOI: 10.1109/JPROC.2011.2131110.

[20] Athanasios Papoulis and S. Unnikrishna Pillai. *Probability, Random Variables, and Stochastic Processes*. 4th. New York, NY, USA: McGraw-Hill, 2002.

AUTHOR

Yi Geng received his B.S. degree from Shandong University in Jinan, China, in 2000, and his M.S. degree from Nanjing University of Posts and Telecommunications in Nanjing, China, in 2007. Since then, he has been actively engaged in the research, development, and customer support of mobile networks from 2G to 6G. Currently, he serves as a researcher in the field of 6G Integrated Sensing and Communications (ISAC) at CICT Mobile, China. His research interests focus on ISAC and non-terrestrial networks.